International Journal of Computational and Experimental Science and ENgineering (IJCESEN)

Vol. 11-No.3 (2025) pp. 7053-7065
http://www.ijcesen.com

ISSN: 2149-9144

Copyright © IJCESEN

Research Article

Model-based optimization of $KGeCl_3$ perovskite solar cells for lead- free inorganic photovoltaic conversion

Hayat Arbouz*

Univerity Saad Dahlab Blida 1, Faculty of Sciences, Physics Department, 09000, Blida-Algeria
* **Corresponding Author Email:** arbouz_hayat@univ-blida.dz - **ORCID:** 0000-0003-2780-5215

Article Info:

DOI: 10.22399/ijcesen.5527
Received : 05 October 2026
Revised : 28 November 2026
Accepted : 30 November 2026

Keywords

Perovskite
Solar Cell
Photovoltaic
Semiconductor
Modelling

Abstract:

The performance and optimization of a perovskite solar cell employing an inorganic, lead- free absorber with a 1.1 eV bandgap were investigated using numerical modeling and simulation. The FTO/TiO_2/$KGeCl_3$/Spiro- OMeTAD/Au, architecture was assessed while layer thicknesses, doping concentrations, and bulk defect densities of the ETL, absorber, and HTL were varied, and while interfacial defect densities at the ETL/absorber and absorber/HTL junctions were modified. Additionally, 36 device configurations combining different ETL and HTL materials were compared. These simulations provided useful information for structural optimization and performance improvement; a maximum conversion efficiency of 21.11% was achieved with the optimized single-junction structure FTO/SnS_2/$KGeCl_3$/MoS_2/Au, and 28.36 % with the $FAPbI_3$/$KGeCl_3$ tandem structure. The potential of $KGeCl_3$ as a lead-free perovskite absorber was thus demonstrated, and the prospects for the future development of sustainable photovoltaic devices were highlighted.

1. Introduction

The evolution of photovoltaic technology toward sustainable energy solutions has unfolded in several phases, ranging from the initial discovery of the photovoltaic effect to current efforts aimed at developing environmentally friendly materials such as perovskites [1]. A major breakthrough occurred in 2012 with the demonstration of the first high-performance solid-state perovskite solar cells, whose efficiency rapidly climbed to 16.2% by the end of 2013. In just a few years, perovskite solar cells have achieved efficiencies of about 26% for single-junction devices and over 33% for tandem configurations [2], positioning them as competitive alternatives to established photovoltaic technologies such as those based on silicon, CdTe, or CIGS. However, research conducted over several years has identified fundamental obstacles that prevent the commercialization of lead-based organo-inorganic hybrid perovskites: insufficient long-term stability, current-voltage hysteresis, and environmental toxicity concerns. Between 2020 and 2023, these major constraints led to in-depth research into alternative lead-free perovskite, particulary those based on tin, germanium, antimony, and bismuth [3], as well as double perovskite structures [4]. Tin-based perovskite solar cells, such as $MASnI_3$, $FASnI_3$, and $CsSnI_3$, have emerged as the most promising lead-free option, as they combine high light absorption with good charge transport, despite the oxidation of Sn^{2+}, which remains a major challenge [5]. Germanium-based devices, such as $CsGeI_3$, have been studied as another lead-free alternative, but their efficiencies have generally remained much lower [6]. Bismuth- and antimony-based materials are of interest because Bi^{3+} and Sb^{3+} ions are more stable in air, but their photovoltaic performance is generally inferior to that of tin-based systems. Examples include $Cs_3Bi_2I_9$, $Cs_2AgBiBr_6$, and $MA_3Sb_2Cl_xI_{(9-x)}$ [7-8-9]. This work focuses on the development of a solar cell based on the perovskite absorber $KGeCl_3$, a lead-free germanium-based material that has recently attracted attention as a promising candidate for photovoltaic applications. The cubic phase of $KGeCl_3$ is particularly appealing for perovskite solar cells because it combines structural stability with favorable optoelectronic properties, including a direct band gap in a useful absorption range, relatively good carrier mobility, low effective mass, and strong visible-light absorption [10]. These characteristics are essential for efficient charge generation, transport, and extraction, and they make $KGeCl_3$ a compelling

absorber for next-generation solar cells. Interest in this material has grown only recently, with a 2023 DFT study identifying $KGeCl_3$ as a promising photovoltaic absorber. Calculations reveal strong optical absorption (>10^5 cm^{-1}), favorable effective masses for both electrons and holes, and low defect formation energies that support efficient charge extraction and direct bandgap, tunable between 1.1 eV and 1.4 eV [11] , closely matches the ideal range for maximizing single-junction solar cell performance under the Shockley–Queisser limit, encouraging device performance under optimized architectures. Indeed, simulations using SCAPS-1D have projected power conversion efficiencies between 17.6% and 21.3% for configurations such as FTO / ZnO/ $KGeCl_3$ / Cu_2O / Au and FTO / TiO_2 /$KGeCl_3$ / Spiro-OMeTAD / Au [12]. Recent theoretical work confirms that $KGeCl_3$ retains its structural phase up to 400 °C and shows no significant decomposition after prolonged ambient exposure, outperforming many Sn- and Pb-based alternatives in stability metrics. Although experimental realizations are still in early stages, successful co-evaporation of phase-pure films with carrier diffusion lengths beyond 500 nm validates its practical synthesizability [13]. Given these optimal properties, $KGeCl_3$ stands out as a high-potential absorber worthy of intensive experimental and theoretical exploration for next-generation sustainable photovoltaics. The configuration and optimization of perovskite solar cells (PSCs) appear as an essential procedure to achieve high photovoltaic efficiency. This is achieved by reducing defect levels, improving optical absorption, minimizing exciton binding energy, and increasing carrier mobility. but also by carefully selecting the neighboring transport layers that play a crucial role not only in the separation and transport of carriers but also in the optimization of band offsets and trap levels at the interfaces, and in the reduction of trap defect levels at the interfaces [14-15-16]. This research used the Mathcad Prime 11 simulation tool to evaluate the photovoltaic performance under various conditions of the $KGeCl_3$-based solar cell structure, employing FTO as the transparent conductive oxide, TiO_2 and Spiro-OMeTAD as ETL and HTL, and gold as the back contact layer. The research included a detailed examination of the optimization of parameters, including the depth, doping density, and defect density of the ETL, the absorption layer, and the HTL, as well as the study of the impact on performance of the defect density level at the ETL/Absorber and Absorber/HTL interfaces. Moreover, an in-depth examination was conducted on 36 structures with different combinations of ETL and HTL materials. After evaluating the PV performance of these configurations, the optimal arrangement of the devices was selected for further development. This numerical analysis provides significant insights regarding the design of efficient and environmentally friendly single and tandem SCs using $KGeCl_3$. The results highlight the capabilities of this type of SC and indicate a pathway for future developments in sustainable solar solutions.

2. Methods

2.1 Device Structure and Methodology

The $KGeCl_3$-based perovskite solar cell (PSC) investigated in this work follows a conventional design with material layers chosen to enhance charge separation and carrier transport. The device stack consists of an aluminum (Al) front contact with a work function of 5.37 eV, a fluorine-doped tin oxide (FTO) transparent window layer, an electron transport layer (ETL) of TiO_2 , the $KGeCl_3$ inorganic and lead-free absorber of 1.1 eV energy of the bandgap, an organic hole transport layer (HTL) of Spiro-OMeTAD , and a gold (Au) rear electrode with a work function of 5.0 eV. The energy levels are arranged such that the $KGeCl_3$ conduction band lies slightly above that of TiO_2 to facilitate downhill electron transfer toward FTO, while its valence band lies above the Spiro-OMeTAD HOMO to enable efficient hole transfer toward Au, thereby establishing a built-in potential between the n-type FTO/TiO_2 side and the p-type Spiro-OMeTAD/ Au side that drives carrier separation and extraction. The complete architecture and energy band alignement of the succesive layers are represented Fig. 1 (a) and (b). Table 1 outlines the input parameters for all materials utilized in the simulation, whereas table 2 details the interface properties of the TiO_2/$KGeCl_3$ and $KGeCl_3$/Spiro-OMeTAD interfaces. The flowchart shown in Fig. 2 outlines the modelling and simulation procedure. The process begins with the definition of the approximate function representing spectral irradiance in this study. Next, the physical parameters of the materials used for the FTO, ETL, perovskite and HTL layers are defined. After that, the expressions used to calculate the photo-current density of electrons and holes, the saturation current density, and the current-voltage characteristic are incorporated into the model. Following that, The device's performance is evaluated based on systematic variations in key parameters: the thicknesses of the absorber, the ETL layer, and the HTL layer, as well as the physical properties—detailed below—of these same layers. This step highlights crucial inter-dependencies, such as how the absorber thickness governs the balance between photon absorption and carrier collection, the

influence of thicknesses on optical transmission, and the interaction between doping and defect states in determining photovoltaic parameters.

Table 1. *Input Simulation Data For FTO, ETL, Absorber and HTL Layers*

Input parameters	FTO [16-17]	TiO_2 [17]	$KGeCl_3$ [12-17]	Spiro-OMeTAD [16]
Thickness, d [nm]	350	100	500	100
Band gap, E_g [eV]	3.50	3.26	1.10	2.20
Electron Affinity, χ [eV]	4.00	4.00	4.00	2.90
Permittivity, ε_r	9	10	23.01	3.00
Electron mobility, μ_n [$cm^2 V^{-1}s^{-1}$]	20	100	92.92	0.02
Hole mobility, μ_p [$cm^2 V^{-1}s^{-1}$]	10	25	68.59	0.0002
CBE effective density of states, N_C [cm^{-3}]	2.2×10^{18}	2.0×10^{17}	6.81×10^{18}	1.0×10^{21}
VBE effective density of states, N_V [cm^{-3}]	1.8×10^{19}	10×10^{17}	3.45×10^{18}	1.0×10^{21}
Density of n-type doping, N_D [cm^{-3}]	1.0×10^{19}	1.0×10^{18}	/	/
Density of p-type doping, N_A [cm^{-3}]	/	/	1.0×10^{12}	1.0×10^{18}
Defect Density N_t [cm^{-3}]	/	1.0×10^{15}	1.0×10^{15}	1.0×10^{15}

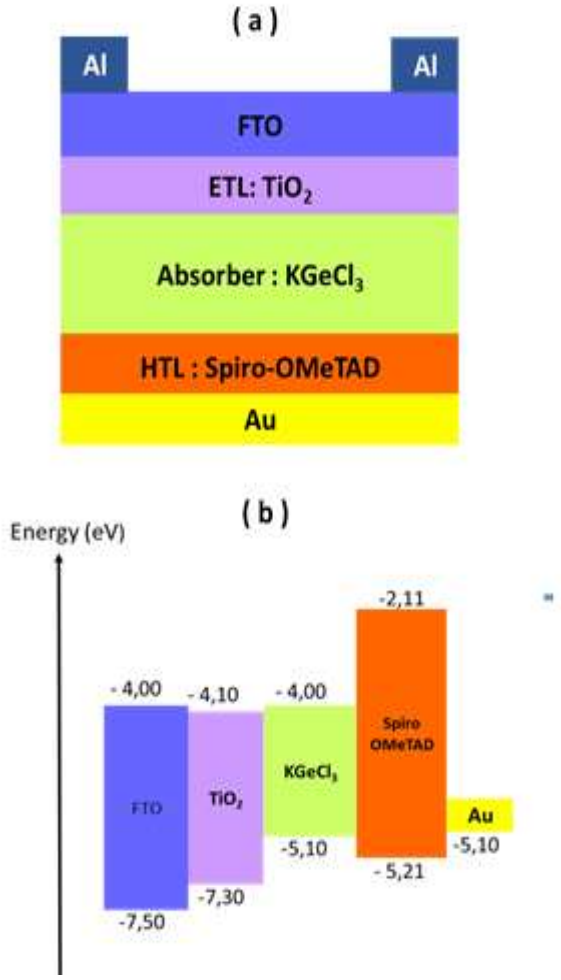


Figure 1. *(a) PSC Structure, (b) Energy Level Diagram.*

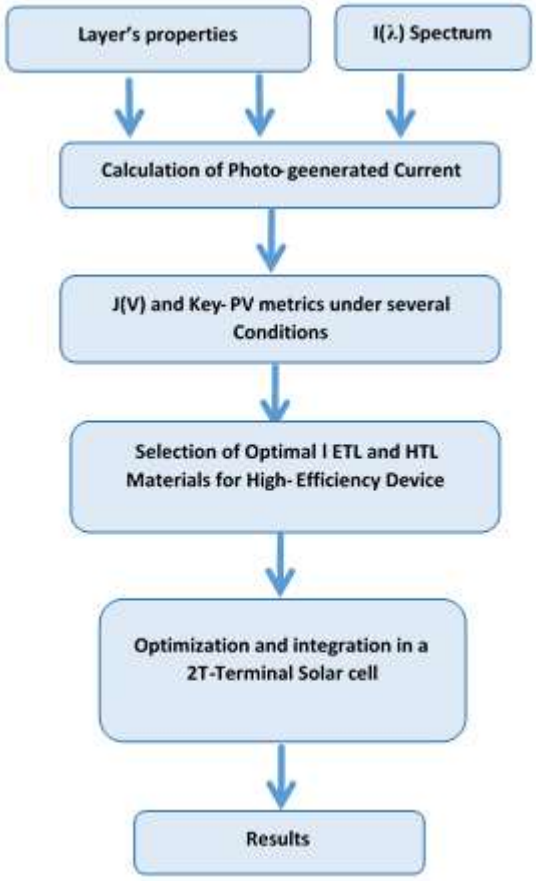


Figure 2. *Simulation Procedure of the Study.*

2.2 Simulation Model

Table 2. *Input parameters for the interface Behaviour* [18].

Parameters	$TiO_2/KGeCl_3$	$KGeCl_3$/Spiro-OMeTAD
Defect mode	Neutral	Neutral
Energetic Distribution	Single	Single
Density of Defect at the Junction, N_t [cm^{-3}]	10^{14}	10^{14}
Defect Energy Position (eV)	0.06	0.06
Electron capture cross section, σ_n [cm^{-2}]	10^{-19}	10^{-19}
Hole capture cross section, σ_p [cm^{-2}]	10^{-18}	10^{-18}

Numerical modeling is an effective methodology for elucidating the operating mechanisms and efficiency limits of photovoltaic devices. Various computational tools have proven to be highly effective in this field. In particular, the one-dimensional solution of the fundamental semiconductor equations provides a rigorous description of the operation of perovskite solar cells. Furthermore, the calculation and analysis of current-voltage characteristics allow for a comprehensive characterization of device performance, encompassing electrical and optical aspects as well as recombination dynamics in multilayer photovoltaic architectures, thereby shedding light on the intrinsic charge transport mechanisms and interfacial phenomena. The study presented here was conducted using Mathcad Prime 11 [19]. The standard conditions generally used in this type of simulation are as follows: the AM 1.5 G solar spectrum with a light intensity of 100 mW/ cm^2, a frequency of 1×10^{16} Hz, and a temperature of 298 K. However, a numerical model of the solar spectrumas a function of the wavelength λ was used in this study. This is the nonlinear equation described in Equation 1 [20].

$$IRS(\lambda) = 0.006977 + 7.0625.[1 - e^{\frac{-(\lambda-0.2605)}{0.15994}}]^{2.28411}.e^{\frac{-(\lambda-0.2605)}{0.22285}} \quad (1)$$

The total power P_{inc} of the incident light, is calculated as follows:

$$P_{inc} = \int_{\lambda_{min}}^{\lambda_{max}} IRS(\lambda) d\lambda \quad (2)$$

The current-voltage characteristics is expressed in Equation 3 [21].

$$J(V) = J_{ph} - (J_0 + J_s).\left(e^{\frac{q.(V - JR_s)}{2kT}} - 1\right) - \frac{V - J.R_s}{R_{sh}} \quad (3)$$

R_s and R_{sh} are parasitic resistances.

J_{ph} is the total photo-current density.

J_0 is the current loss arising from non- radiative recombination and depends on the carrier density, carrier lifetimes, and diffusion coefficients. J_s is the current loss associated with interface recombination and is determined by the interface defect density and the band energy-level mismatch [22]. Generating the J(V) curve requires an accurate assessment of absorption, recombination and length's diffusion; to this end, the Tauc model [23- 24] was used to calculate absorption, and the Shockley-Read-Hall (SRH) formula [25] was used to estimate the recombination rate. Their corresponding expressions are given by Equations 4 and 5.

$$\alpha(h\nu) = (\alpha_0 + \beta_0.\frac{E_g}{h\nu}).\sqrt{\frac{h\nu}{E_g} - 1} \quad (4)$$

hν is the photon energy.

α_0 and β_0 are the model constants that depend on the standard model constants A and B:

$$\alpha_0 = A\sqrt{E_g} \quad \text{and} \quad \beta_0 = \frac{B}{\sqrt{E_g}}$$

$$R_{SRH} = \frac{(n.p - {n_i}^2)}{\tau.(p + n + 2.n_i.cosh(\frac{E_i - E_t}{k_B.T}))} \quad (5)$$

R_{SRH} is SRH rate which depends on the life-time of the minority carrier (τ) and the defect density N_t.

$$\tau = \frac{1}{N_t.\sigma.V_{th}} \quad (6)$$

E_t is the position of the trap energy level and the intrinsic level is represented by E_i. T is the absolute temperature. k_B is the Boltzmann constant. $\sigma_{n,p}$ is the capture cross-section for electrons or holes, N_t is the defect density and the V_{th} is the thermal speed.

The following Equation illustrates the strong relationship between the diffusion length as a function of diffusion's coefficient and carrier lifetime:

$$L_{(n,p)} = \sqrt{\tau_{(n,p)}.D_{(n,p)}} \quad (6)$$

The coefficient of diffusion, diffusion length, and minority carrier lifetime are denoted $D_{(n,p)}$, $L_{(n,p)}$, and $\tau_{(n,p)}$, respectively. Equations 7 and 8 define the fill factor and the power conversion efficiency, respectively [26].

$$FF = \frac{J_{mp}.V_{mp}}{J_{SC}.V_{oc}} \quad (7)$$

J_{mp} is the maximum current and V_{mp} is the maximum voltage. J_{sc} and V_{oc} are short current density and open circuit voltage respectively.

$$PCE = \frac{J_{mp}.V_{mp}}{P_{inc}} \quad (8)$$

3. Results, Discussion and Optimization

3.1 Optimization of $KGeCl_3$ Layer Thickness, Doping Density, and Defect Density for Improved Performance

The key physical parameters of a solar cell's absorbing layer, which govern and ensure optimal charge carrier generation, are the acceptor density (N_a), the trap density (Nt), and the thickness of the active layer. Optimizing these parameters is essential for improving the efficiency of solar devices. Fig. 3 (a) illustrates the effect of the doping level in the $KGeCl_3$ layer on the current-voltage (J-V) characteristic curve. It is observed that at moderate levels—generally between 10^{13} and 10^{19} cm^{-3}—doping increases the built-in potential at the p-n junction, which facilitates efficient separation of electrons and holes and increases the open-circuit voltage (V_{oc}) from 0.4956 V to 0.6719 V, thereby minimizing non-radiative recombination pathways. On the other hand, the short-circuit current density (J_{sc}) remains stable due to the extended carrier lifetime, resulting in a better fill factor (FF). Conversely, excessive doping beyond 10^{19} cm^{-3} has a detrimental effect that promotes Auger and Shockley-Read-Hall recombination, narrows the space charge region, and strengthens interface traps. Fig. 3 (b) illustrates the effect of defect density on the device's current-voltage J(V) curve. It is clear that at low defect densities, below 10^{13} cm^{-3}, performance is high due to reduced Shockley-Read-Hall (SRH) recombination, extended carrier lifetimes, and an optimal built-in potential. This maintains high open-circuit voltage (V_{oc}), short-circuit current density (J_{sc}), and fill factor (FF). Conversely, a high level of trap defects, exceeding10^{14} cm^{-3} , promotes SRH and Auger-type recombination, shortens the lifetime of minority carriers, and narrows the space charge region. This results in a degradation of V_{oc} from 0.6491 V to 0.1731 V, a decrease of J_{sc} from 35.65 mA/cm² to 0.009 mA/cm² and, as a result, a significant decrease in FF and energy conversion efficiency due to a substantial increase in non-radiative losses. The perovskite $KGeCl_3$ possesses excellent light absorption properties and high carrier mobility; however, the results above clearly show that its performance is affected by a high defect density. Consequently, optimizing its thickness is crucial because it strongly influences the light absorption rate and carrier generation. Fig. 3 (c) shows the impact of the $KGeCl_3$ absorber thickness on the device's J(V) curve. The latter shows a greater influence on the short-circuit current, which increases from 29.94 mA/cm² to 38.36 mA/cm² as the thickness increases from 250 nm to 1.45 µm, than on the open-circuit voltage, which increases from 0.5742 V to 0.5838 V for the same variation. This results in an increase in the fill factor (FF) and conversion efficiency, which reach 76.5 % and 18.28 %. However, beyond a thickness of 1.45 µm, the improvement in performance slows down, until it reaches a plateau at a thickness of 1.55 µm, then begins to decrease slightly.

3.2 Impact of Interfacial Density of Defects at ETL/perovskite and perovskite/HTL regions

Perovskite solar cells face significant efficiency limitations due to defective interfaces and suboptimal band alignment between the perovskite and the electron transport (ETL) and the hole transport (HTL) layers. These defects intensify charge recombination pathways, which adversely affect key performance parameters: power conversion efficiency (PCE), open-circuit voltage (V_{oc}), short-circuit current density (J_{sc}), andThis study systematically evaluates interfacial trap state density (N_{int}) effects at the TiO_2 /$KGeCl_3$ fill from 10^{12} cm^{-3} (minimal) to 10^{20} cm^{-3} (severe) .

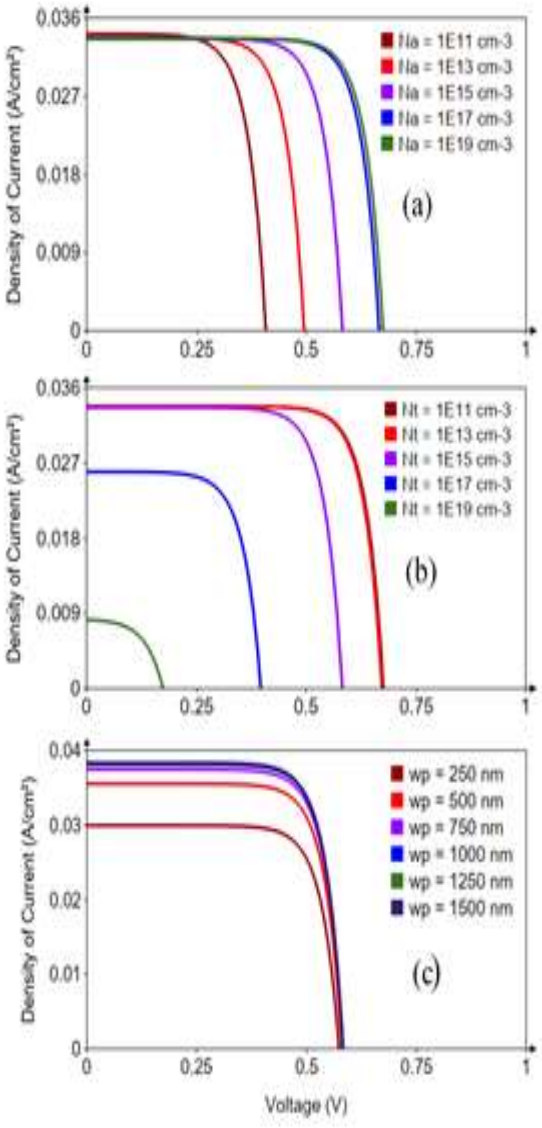


Figure 3. *Impact of (a) Density of Acceptors, (b) Density of Defects, (c) Thickness of the Absorber ,on J(V) curve of $KGeCl_3$ -based PSC.*

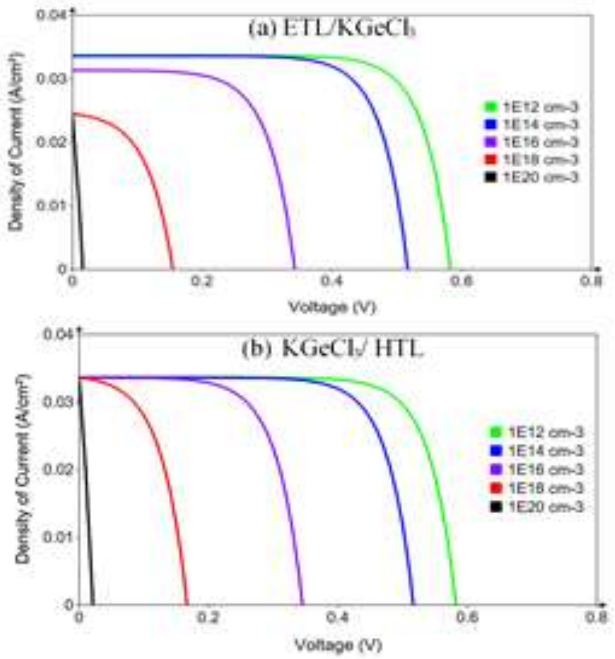


Figure 4. *Impact of (a) Density of defects at ETL/$KGeCl_3$ Interface, (b) Density of Defects at $KGeCl_3$/HTL Interface, on J(V) characteristic's.*

anode-side and $KGeCl_3$ /Spiro-OMeTAD cathode-side contacts. Figure 4. (a) and (b) display measured J(V) characteristics across N_{int} from 10^{12} cm^{-3} (minimal) to 10^{20} cm^{-3} (severe). High N_{int} establishes traps that exponentially increasing surface recombination velocity and depleting extractable carriers. Simulations predict a sharp PCE decline past 10^{15} cm^{-3} (ETL interface).At the ETL/absorber junction, imperfections create localized trapping states within the bandgap. These traps can capture electrons and holes from the perovskite, leading to Shockley-Read-Hall (SRH) recombination. Since the ETL/absorber interface is generally the first charge extraction interface, recombination at this location is particularly detrimental compared to defects present in the bulk or even on the absorber/HTL side in many structures. This introduces a surface recombination rate that varies in proportion to the defect density and the effective trapping cross-section of the traps. Fig 4. (a) shows the effect of the defect density at the interface between the ETL layer and the $KGeCl_3$ absorber layer. It is observed that the short-circuit current density and open-circuit voltage begin to decrease only starting at 10^{14} cm^{-3} and 10^{12} cm^{-3} respectively. A decrease in J_{sc} from 33.64 mA/cm² to 24.20 mA/cm² and in Voc from 0.5824 V to 0.00101 V is observed when the defect density at ETL/$KGeCl_3$ increases from 10^{12} cm^{-3} to 10^{20} cm^{-3}, which indicates that high densities of interface defects at the ETL/absorber junction lead to a drop in the V_{oc} and reduce the number of carriers contributing to the external photo-current, leading to a decrease in J_{sc}. However, the high defect density at the interface between $KGeCl_3$ and the HTL, shown on Fig 4. (b), has no effect on J_{sc}. In fact, although holes recombine at this interface, the photo-current which consists mainly of photo-generated electrons is not affected. However, the V_{oc} undergoes a significant decrease from 0.5824 V to 0.0014 V when the defect density at $KGeCl_3$/HTL interface increases from 10^{12} cm^{-3} to 10^{20} cm^{-3}. The above mentioned investigation suggests that reduced defect density in these areas ensures optimal cell performance.

3.3 ETL and HTL Thickness and Doping Density Effects on $KGeCl_3$ Solar Cell Power Conversion Efficiency

In perovskite solar cells (PSCs), the donor density (N_D) and the thickness of the electron transport layer (ETL) are crucial parameters that directly govern charge extraction, recombination dynamics, and

Table 4. *Photovoltaic performance of $KGeCl_3$ Solar Cell based on optimal ETL and HTL Combinations*

Structure	E_g (eV)	J_{ph}(mA/cm²)	V_{oc} (V)	FF(%)	PCE (%)
FTO/TiO_2/$KGeCl_3$/S-O/Au -This work	1.10	33.64	0.5824	76.51	15.99
FTO/SnS_2/$KGeCl_3$/MoS_2/Au - This work	1.10	38.82	0.6522	78.17	21.11
ITO/IGZO/$KGeCl_3$/V_2O_5/Au [34] SIM	1.10	/	/	/	21.23
FTO/TiO_2/$KGeCl_3$/Cu_2O/Au [35] SIM	1.10	/	/	/	29.03
FTO/TiO_2/$MASnI_3$/CZTS/Au [36]-EXP	1.25	20.31	0.94	72.00	13.75
FTO/TiO_2 /$MASnI_3$ /CBTS/Au [37]-SIM	1.25	30.24	1.03	83.41	25.86

Table 5. *Photovoltaic performance of the Optimized $KGeCl_3$ Solar Cell Structure.*

Structure	E_g (eV)	J_{ph}(mA/cm²)	V_{oc} (V)	FF(%)	PCE (%)
FTO/TiO_2/$KGeCl_3$/S-O/Au -This work	1.10	33.64	0.5824	76.51	15.99
FTO/SnS_2/$KGeCl_3$/MoS_2/Au - This work	1.10	38.82	0.6522	78.17	21.11
ITO/IGZO/$KGeCl_3$/V_2O_5/Au [34] SIM	1.10	/	/	/	21.23
FTO/TiO_2/$KGeCl_3$/Cu_2O/Au [35] SIM	1.10	/	/	/	29.03
FTO/TiO_2/$MASnI_3$/CZTS/Au [36]-EXP	1.25	20.31	0.94	72.00	13.75
FTO/TiO_2 /$MASnI_3$ /CBTS/Au [37]-SIM	1.25	30.24	1.03	83.41	25.86

Table 6. *Photovoltaic performance of Tandem Structures Based on $KGeCl_3$ Bottom Subcell.*

Structure	E_{gT}/E_{gB} (eV)	w_T/w_B(nm)	J_{ph}(mA/cm²)	V_{oc} (V)	FF(%)	PCE(%)
2T-Tandem 1 (This work)	1.55/1.10	800/206	16.15	1.797	86.6	26.82
2T-Tandem 2 (This work)	1.51/1.10	800/189	17.33	1.773	86.53	28.36
2T - Tandem 3 (This work)	1.60/1.10	800/166	14.50	1.889	64.17	24.64
Si/Perovskite-Planar (Simulation) [38]	1.12/1.55	/	19.81	1.772	77.42	27.17
Si/Perovskite-Nanotextured (Simulation) [38]	1.12/1.55	/	21.12	1.772	77.97	28.97
Si/Perovskite-Planar (Experiment) [38]	1.12/1.55	/	19.02	1.773	78.02	26.31
Peroskite/Perovskite (Experiment) [39]	1.25/1.75	/	/	/	/	22.90

intrinsic potential, thereby determining the power conversion efficiency (PCE). An appropriate donor density promotes the efficient extraction of light-generated electrons and improves charge mobility and separation. At the same time, the thickness of the ETL must be carefully optimized. A thickness greater than 100 nm increases stray absorption and series resistance, which reduces electron extraction efficiency, the fill factor (FF), and current density, while an ETL that is too thin (< 20 nm) may result in incomplete coverage of the perovskite, the formation of interface traps, and shunting. The optimal combination of high donor density and a low-to-moderate ETL thickness maximizes the V_{oc}, J_{sc}, and FF values, thereby enabling a high PCE. Fig. 5 shows the contour plot of the conversion efficiency of the $KGeCl_3$ cell as a function of the simultaneous variation in the depth of the ETL layer of the base structure, TiO_2, from 50 nm to 550 nm. Analysis has shown that thickness has no significant influence on conversion efficiency regardless of donor concentration. However, the optimal conversion efficiency is observed at a donor concentration between 10^{12} however, the optimal conversion efficiency is observed at a donor concentration between 10^{12} cm^{-3} and 10^{16} cm^{-3} with values ranging

from 17.47% to 18.72%. Conversion efficiency begins to decline beyond this range. Fig. 6 shows the conversion efficiency of the $KGeCl_3$-based solar cell as a function of TiO_2 electron transport layer (ETL) thickness (50–550 nm) and ETL donor concentration. Across the full thickness range examined, the conversion efficiency is essentially invariant with ETL thickness, indicating that, within these bounds, optical absorption and carrier transport through the TiO_2 layer do not limit device performance. In contrast, efficiency depends strongly on the ETL donor concentration. The device reaches peak performance for donor concentrations between 10^{12} and 10^{16} cm^{-3}, where the power conversion efficiency (PCE) lies between 17.47% and 18.72%. Outside this concentration ndow the PCE falls off, with more pronounced reductions at concentrations above 10^{16} cm^{-3}. These observations can be explained by competing effects of charge extraction and recombination governed by the ETL doping level. At low donor concentrations ($<10^{12}$ cm^{-3}), the ETL conductivity is limited, which increases series resistance and impairs electron extraction. This leads to lower short-circuit current density (J_{sc}) and fill factor (FF), reducing the overall PCE. In the optimal mid-range (10^{12}–10^{16} cm^{-3}), the ETL provides sufficient conductivity for efficient electron transport while maintaining favorable band alignment and low recombination losses at the ETL/absorber interface, producing the observed maximal efficiencies. At high donor concentrations ($>10^{16}$ cm^{-3}), increased free-carrier density can shift the TiO_2 Fermi level, modify the band bending at the interface, and enhance inter-facial recombination

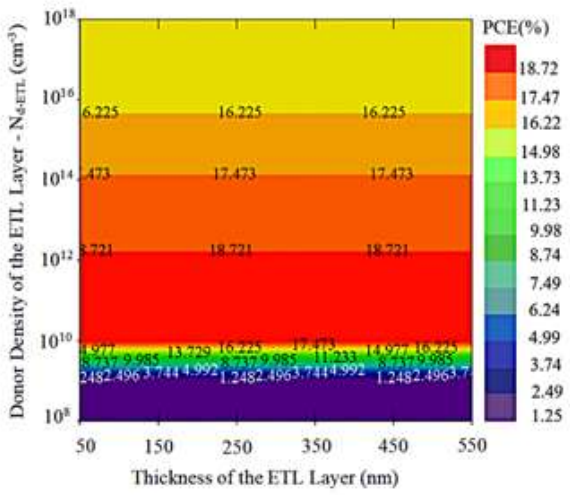


Figure 5. *Impact of ETL Donor Density and Defect Density on the Performance of $KGeCl_3$ Solar Cell.*

(via higher trap-assisted recombination or increased Auger-type processes in extreme cases), which together reduce open-circuit voltage (V_{oc}) and FF and therefore lower PCE. The negligible sensitivity to ETL thickness suggests that, for this $KGeCl_3/TiO_2$ architecture, light absorption is dominated by the absorber layer and not significantly affected by interference or parasitic absorption in the ETL over the studied thickness range.Furthermore, the concentration of Na acceptors in the hole transport layer (HTL) and its thickness are equally critical parameters that govern hole extraction, the recombination rate at the perovskite/HTL interface, and the intrinsic potential, thereby directly determining the power conversion efficiency (PCE). A high Na concentration improves hole mobility and the separation of light-generated holes. At the same time, the thickness of the HTL must be carefully optimized: a thickness greater than 400 nm reduces hole mobility and transport. Conversely, an HTL that is too thin (< 100 nm) carries the risk of interface traps and increased recombination at the HTL/perovskite interface. The optimal balance between these two factors leads to high performance. Fig.6 shows a contour plot illustrating the conversion efficiency of the $KGeCl_3$-based perovskite solar cell as a function of HTL layer thickness (50–550 nm) and acceptor density (10^{10}–10^{18} cm^{-3}). The results reveal a maximum efficiency (~16%) within a broad operating window defined by a thickness between 100 and 500 nm, combined with an acceptor density greater than $10^{14}cm^{-3}$. This high-efficiency region indicates that the device tolerates significant variations in HTL layer thickness while maintaining optimal performance, provided that the acceptor density remains sufficiently high to ensure adequate hole conductivity and intrinsic potential. Conversely, the efficiency drops considerably when either of these parameters falls below these thresholds: acceptor densities below 10^{14} cm^{-3} result in insufficient hole extraction and increased recombination due to poor conductivity of the HTL layer, while thicknesses below 100 nm lead to incomplete coverage of the perovskite and a higher density of interface traps, which degrade both the fill factor and the current density. This distribution thus identifies 10^{14} cm^{-3} as the critical acceptor density threshold and 100 nm as the minimum viable thickness of the HTL layer for achieving high-performance $KGeCl_3$-based cells.

3.4 Enhancing Solar Cell Performance Through ETL and HTL Optimization

It is well known that ETLs primarily serve to capture electrons from the absorber layer and efficiently transport them to the front electrode, while hindering the flow of holes to reduce interfacial recombination. Conversely, HTLs promote the extraction and transfer of holes to the back contact, thereby

facilitating efficient charge separation and circuit closure [27].

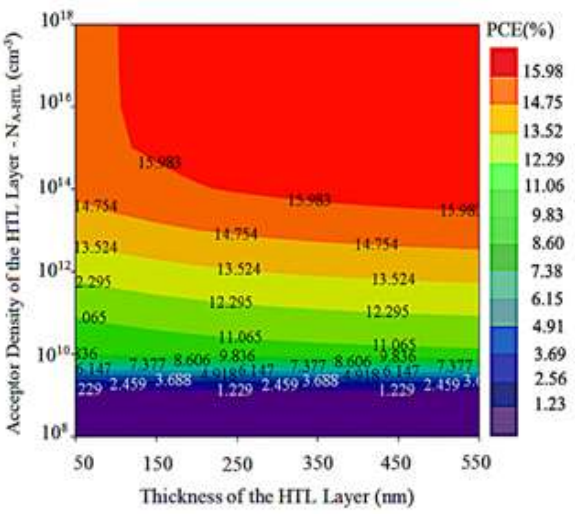


Figure 6. *Impact of HTL Acceptor Density and Defect Density on the Performance of $KGeCl_3$ Solar Cell.*

Therefore, the improvement in PSC efficiency is primarily attributed to the integration of optimized ETL and HTL layers. This section discusses the evaluation of the photovoltaic performance of optimal combinations of ETLs and HTLs for the $KGeCl_3$ perovskite solar cell. Six ETLs (TiO_2, SnO_2, SnS_2, ZnMgO, C60, and WS_2) were combined with five HTLs (Spiro-OMeTAD (S-O), PEDOT:PSS (P:PSS), Cu_2O, CuSCN, NiO, and MoS_2), resulting in 36 different structural configurations. Key photovaltaic metrics of the structures shown in Fig.7. Among the architectures studied, two combinations stand out in particular. These are the SnS_2-based ETL structures and the Cu_2O- and MoS_2-based HTL structures, which achieved the highest conversion efficiencies of 17.1% highlighting strong alignment at the interfaces with the $KGeCl_3$ absorber layer. Detailed data on the performance of these two structures are presented in table 4. The conduction- and valence-band offsets between the perovskite layer and the ETL/HTL materials are listed in the table. These results indicate that SnS_2 is the most promising ETL: its band alignment with $KGeCl_3$ is the same Cliff-type barrier observed for TiO_2, but the offset is slightly larger, with an energy difference of −0.26 eV. Although Cu_2O and MoS_2 HTLs produced the same conversion efficiency, MoS_2 showed superior valence-band alignment with the absorber. Consequently, the $SnS_2/KGeCl_3/MoS_2$ ETL/perovskite/HTL architecture is selected as optimal.

3.5 Manufacturing Considerations and Key Advantages of the Proposed Architecture

The $FTO/SnS_2/KGeCl_3/MoS_2/Au$ perovskite solar cell architecture presents a compelling, fully inorganic, lead-free alternative to the conventional $FTO/TiO_2/KGeCl_3/Spiro\text{-}OMeTAD/Au$ configuration, offering synergistic advantages in charge transport, stability, fabrication, and environmental compatibility. SnS_2 serves as an efficient ETL that aligns well with $KGeCl_3$, minimizing interfacial recombination and voltage losses, while MoS_2 functions as a robust, inorganic HTL that enables strong hole extraction without

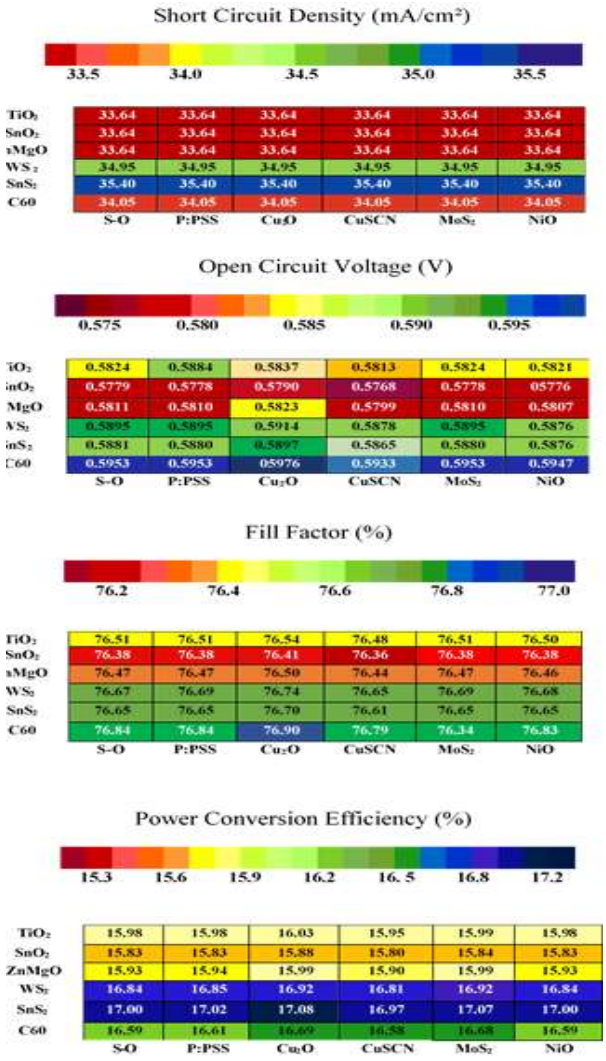


Figure 7. *Key Photovoltaic Metrics of $KGeCl_3$ Solar Cell Structures with different combinations of ETL and HTL materials.*

requiring hygroscopic dopants which are essential for Spiro-OMeTAD but introduce moisture sensitivity, ionic migration, and interfacial instability [28].

From a stability standpoint, SnS_2 does not catalyze perovskite degradation under illumination, unlike TiO_2 , which is a well-known photocatalyst that accelerates organic/inorganic perovskite decomposition in the presence of oxygen and

moisture [29], while both SnS_2 and MoS_2 exhibit thermal robustness well above 200 °C, in stark contrast to Spiro-OMeTAD, which undergoes morphological changes or decomposition at temperatures above 85 °C [30].

Fabrication benefits are equally pronounced: SnS_2 can be deposited at room temperature via vacuum deposition, chemical bath deposition, or spin-coating [31], whereas TiO_2 typically requires high-temperature sintering (>450 °C) that limits substrate choice and increases energy costs; MoS_2 can be processed via solution-based spin-coating process or low-temperature CVD (<300 °C) [32], avoiding the high-vacuum thermal evaporation often needed for high-quality Spiro-OMeTAD films, and both SnS_2 and MoS_2 function effectively without chemical dopants allowing air-processable fabrication with minimal performance loss.

The morphology of SnS_2 and MoS_2 yields conformal, pinhole-free films that reduce shunting pathways, unlike TiO_2 and Spiro-OMeTAD, which often require additional compact layers or surface passivation.

At the absorber level, $KGeCl_3$ offers superior intrinsic stability compared to hybrid perovskites with similar effective bandgaps (e.g., low-gap Sn/Pb mixed systems), as it lacks volatile organic cations, exhibits high resistance to moisture-induced degradation, and avoids UV-induced photocatalytic decomposition mediated by organic species. $KGeCl_3$ also maintains its photoactive phase under continuous illumination, unlike $FAPbI_3$, and it avoids both Pb toxicity and Sn^{2+} oxidation instability [33], making it uniquely suitable for infrared-absorbing bottom cells in tandem architectures enabling theoretical efficiencies exceeding 30%. Collectively, these attributes position the FTO/SnS_2/$KGeCl_3$/MoS_2/Au stack as a uniquely robust, manufacturable, and environmentally benign platform for next-generation narrow-gap perovskite photovoltaics.

4. Performance of $KGeCl_3$-Based Optimized Solar Cell Devices: Single and Tandem Designs

After evaluating the effects of all the parameters studied, the final optimization was performed by adjusting these variables within the limits imposed by the experimental setup. The optimized device has an ETL thickness of 50 nm, an absorber thickness of 1.70 µm, and an HTL thickness of 300 nm. The defect density of the absorber was set to 10^{14} cm^{-3}, with interface defect densities of 10^{12} cm^{-3}at the ETL/absorber and absorber/HTL interfaces. The doping densities were 10^{15} cm^{-3} for the ETL and 10^{18} cm^{-3}, for the HTL. Under these conditions, the cell efficiency reached 21.11%. Detailed performance metrics are presented in Table 5.

Compared with the baseline device, which exhibited a conversion efficiency of only 15.99%, the optimized structure achieved a value of 21.11%, corresponding to an absolute increase of 5.12%. In addition, all photovoltaic parameters were improved, reaching 38.82 mA/cm² for J_{sc}, 0.6522 V for V_{oc}, and 78.17% for FF, which represent increases of 5.18 mA/cm², 0.0698 V, and 1.66%, respectively. Reference [34] reported a close yield of 21.23% using IGZO and V_2O_5 as ETL and HTL repectivelly. A relative error of 0.005 in conversion efficiency was found between that report and the current work, likely attributable to differences in simulation methodology and the parameters considered.

In Reference [35], where TiO_2 and Cu_2O were employed as the electron- and hole-transport layers, respectively, an efficiency of 29.03 % was reported; this value exceeds the result obtained here, probably due to differing simulation approaches and underlying assumptions. Compared with devices based on the hybrid, lead-free perovskite $MASnI_3$, whose bandgap is about 1.25 eV and is slightly larger than that of $KGeI_3$, the experimental device reported in Reference achieved a power conversion efficiency of only 13.75%. This lower value is attributable to realistic fabrication conditions, which typically yield efficiencies below theoretical predictions, whereas a simulated device in another study reached 25.86%.

The optimized device based on a low-bandgap absorber can also be implemented as the rear subcell in a tandem structure, provided it is combined with a compatible wide-bandgap top cell. It should be emphasized that the most successful perovskite tandems reported so far generally use a silicon bottom junction together with a lead-containing hybrid perovskite top junction, for example $MAPbI_3$. All-perovskite tandems, however, have not yet reached comparable efficiencies. In these systems, the narrow-bandgap layer is often composed of $MASnI_3$ or $CsSnI_3$; the former is unstable due to its organic component, which is sensitive to heat and humidity, while the latter is entirely inorganic and therefore more thermally stable. However, both compounds are prone to degradation due to tin oxidation, which compromises their long-term operational performance. Consequently, $KGeCl_3$ is a promising substitute: it has a bandgap identical to that of silicon and exhibits greater chemical stability than tin-based perovskites.

The final part of this study involves evaluating the potential of the optimized $KGeCl_3$-based subcell as the bottom layer of a tandem device architecture. Three tandem structures were investigated.

The two-terminal tandem configuration was considered. A 2T-Tandem solar cell stacks two subcells in series—one with a narrow bandgap and the other with a wider bandgap—and connects them via an internal recombination layer, so that the same current flows through both devices [38]. The main design challenge lies in current matching: the top cell must absorb high-energy photons while remaining as transparent as possible to the lower-energy light intended for the bottom cell; furthermore, the thicknesses and bandgaps must be optimized to minimize resistive and optical losses.

The performance of three tandem structures was simulated in the final section of this study. These structures share a common bottom section consisting of an optimized 800 nm-thick $KGeCl_3$ layer for the bottom subcell, while their top subcell sections differ. Structures 1, 2, and 3 use $MAPbI_3$, $FAPbI_3$, and $CsGeI_3$, respectively, with band gaps of 1.55, 1.51, and 1.60 eV for the upper subcells. Since a two-terminal (2T) tandem configuration was considered, the thickness of the top absorber was adjusted for each structure so that the current densities of the two subcells were matched. A current-matching analysis was therefore performed. Fig. 8 shows the current-voltage characteristics of the tandem structures, and the main photovoltaic parameters are listed in Table 6.

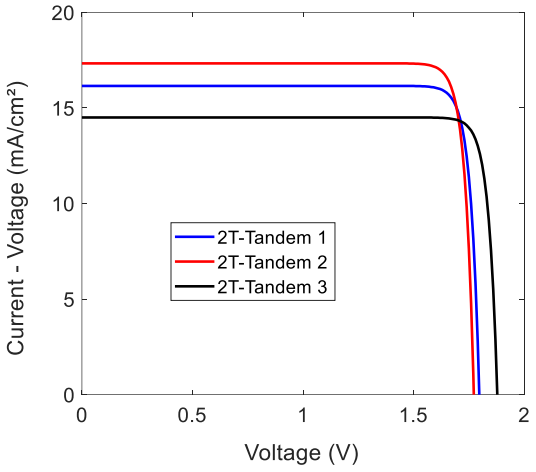


Figure 8. *Current-Voltage Curve of $KGeCl_3$-based Tandem Solar Cell Structures.*

The results show that the $KGeCl_3$ /$FAPbI_3$ (2T-tandem 2) structure achieved the highest power conversion efficiency, reaching 28.36%, among the three simulated configurations with lower- and upper-cell absorber thicknesses of 800 nm and 189 nm, respectively. This result indicates a favorable bandgap alignment between the two subcells, with bandgaps of 1.10 eV and 1.51 eV, which enables effective spectral splitting and efficient utilization of the incident light. In contrast, as the bandgap of the upper subcell increases, the conversion efficiency decreases because the energetic mismatch between the two subcells becomes larger. Consequently, the $KGeCl_3$/$MAPbI_3$ and $KGeCl_3$/$CsGeI_3$ (2T-Tandem 1 and 3) structures reached efficiencies of 26.82% and 24.64%, respectively.

Moreover, the performance achieved in this work is comparable to that reported in the references listed in Table 6 for tandem solar cells based on silicon and conventional $MAPbI_3$ perovskite. This highlights the strong potential of $KGeCl_3$—a thin, non-toxic, and low-cost material—as a promising alternative to thick silicon, whose fabrication is more complex, in tandem photovoltaic devices.

5. Conclusion

In summary, the present work identifies $KGeCl_3$ as a viable lead-free perovskite absorber for photovoltaic applications, owing to its direct band gap of 1.1eV and characteristics indicating that $KGeCl_3$ can support efficient photon absorption, charge separation, and carrier transport while offering a more sustainable alternative to conventional Pb- and Sn-based absorbers. Device-level optimization further shows that the photovoltaic response is strongly governed by transport-layer selection and interfacial quality. Through numerical evaluation of 36 architectures, the SnS_2/$KGeCl_3$/MoS_2 configuration emerged as the most favorable design, primarily because of improved band alignment at the absorber/HTL interface. Relative to the unoptimized device, whose efficiency was 15.99%, the optimized structure delivered 21.11% power conversion efficiency, corresponding to an absolute increase of 5.12 %. This enhancement was accompanied by an increase in short-circuit current density from 33.64 to 38.82 mA/cm², an open-circuit voltage rise from 0.5824 to 0.6522 V, and a fill factor improvement from 76.51% to 78.17%.

Furthermore, the simulation results show that the $KGeCl_3$/$FAPbI_3$ two-terminal tandem solar cell offers a power conversion efficiency (PCE) of 28.36% for absorber thicknesses of 800 nm and 189 nm for the bottom and top cells, respectively. This exceptional result is due to an effective bandgap matching: 1.10 eV for $KGeCl_3$ and 1.51 eV for $FAPbI_3$. The efficiency achieved is comparable to that of previously reported Si/perovskite tandem devices, highlighting the potential of $KGeCl_3$ as a thin, lead-free, and low-cost alternative to thick silicon in tandem architectures.

The findings therefore suggest that $KGeCl_3$ is not only theoretically attractive but also strategically suitable for further development in single-junction and tandem solar-cell concepts. At the same time, the results underline the importance of reducing defect

densities, refining interfacial energetics, and validating the proposed design experimentally. Taken together, the study provides a strong basis for future investigations aimed at translating the favorable intrinsic properties of $KGeCl_3$ into practical high-efficiency photovoltaic devices.

Author Statements:

- **Ethical approval:** The conducted research is not related to either human or animal use.
- **Conflict of interest:** The authors declare that they have no known competing financial interests or personal relationships that could have appeared to influence the work reported in this paper
- **Acknowledgement:** The authors declare that they have nobody or no-company to acknowledge.
- **Author contributions:** The authors declare that they have equal right on this paper.
- **Funding information:** The authors declare that there is no funding to be acknowledged.
- **Data availability statement:** The data that support the findings of this study are available on request from the corresponding author. The data are not publicly available due to privacy or ethical restrictions.

References

[1]Al-Ali, S., Olabi, A. G., & Mahmoud, M. (2025). A review of solar photovoltaic technologies: Developments, challenges, and future perspectives. *Energy Conversion and Management: X*. 27:101057. DOI:10.1016/j.ecmx.2025.101057

[2]Jeong, J., Kim, M., Seo, J., et al. (2021). Pseudo-halide anion engineering for α-$FAPbI_3$ perovskite solar cells. *Nature*. 592:381-385. DOI:10.1038/s41586-021-03406-5

[3]Xiao, J., et al. (2023). Development of lead-free perovskite solar cells: Properties, opportunities and challenges. *Renewable and Sustainable Energy Reviews*. 189:113926. DOI:10.1016/j.rser.2023.113926

[4]Mohandes, A., & Moradi, M. (2025). Achieving 27.20% efficiency for a lead-free double perovskite solar cell with all inorganic Cs_2BiAgI_6 using AZO UTL as a passivation layer. *Materials Advances*. 6(4):1520-1539. DOI:10.1039/D4MA01280A

[5]Mahmud, M. A., Duong, T., Peng, J., Wu, Y., Shen, H., Walter, D., Nguyen, H. T., Mozaffari, N., Tabi, G. D., Cathro, M., Grant, D. E., Mahmud, M. A. H., White, T. P., Weber, K., & Catchpole, K. (2020). Origin of efficiency loss and stabilization strategies in tin-based perovskite solar cells. *Advanced Functional Materials*. 30(49):2005081. DOI:10.1002/adfm.202005081

[6]Krishnamoorthy, T., Ding, H., Yan, C., Leong, W. L., Baikie, T., Zhang, Z., Sherburne, M., Li, S., Asta, M., Mathews, N., & Mhaisalkar, S. G. (2015). Lead-free germanium iodide perovskite materials for photovoltaic applications. *Journal of Materials Chemistry A*. 3(47):23829-23832. DOI:10.1039/C5TA05741H

[7]Hamukwaya, S. L., Hao, H., Mashingaidze, M. M., Zhong, T., Tang, S., Dong, J., Xing, J., & Liu, H. (2022). Potassium iodide-modified lead-free $Cs_3Bi_2I_9$ perovskites for enhanced high-efficiency solar cells. *Nanomaterials*. 12(21):3751. DOI:10.3390/nano12213751

[8]Alsalme, A., Khan, R. A., Altowairqi, M. F., & Almuryyi, N. A. (2023). Theoretical and experimental study of methyl ammonium antimony iodide-based lead-free perovskite solar cells. *Energies*. 16(1):236. DOI:10.3390/en16010236

[9]Aina, S., Villacampa, B., & Bernechea, M. (2021). Earth-abundant non-toxic perovskite nanocrystals for solution processed solar cells. *Materials Advances*. 2(13):4140-4151. DOI:10.1039/d1ma00245g

[10]Abbasi, Z., Jan, S. T., Safeer, M., Imran, M., & Rehman, A. U. (2025). Optimization & enhancement of $KGeCl_3$-based perovskite solar cells through charge transport layer engineering. *RSC Advances*. 15:2525-2544. DOI:10.1039/d4ra08299k

[11]Namisi, M. M., Musembi, R. J., Mulwa, W. M., & Aduda, B. O. (2023). DFT study of cubic, tetragonal and trigonal structures of $KGeCl_3$ perovskites for photovoltaic applications. *Computational Condensed Matter*. 34:e00772. DOI:10.1016/j.cocom.2022.e00772

[12]Tarekuzzaman, M., Ishraq, M. H., Parves, M. S., Rayhan, M. A., Ahmad, S., Rasheduzzaman, M., Al Mamun, K. A., Hossen, M. M., & Hasan, M. Z. (2024). An in-depth investigation of lead-free $KGeCl_3$ perovskite solar cells employing optoelectronic, thermomechanical, and photovoltaic properties: DFT and SCAPS-1D frameworks. *Physical Chemistry Chemical Physics*. 26(39):27704-27734. DOI:10.1039/d4cp02974g

[13]Sarhani, M. E., Dahame, T., Belkhir, M. L., Bentria, B., & Begagra, A. (2023). Ab-initio study of electronic, mechanical, optical and thermoelectric properties of $KGeCl_3$ for photovoltaic application. *Heliyon*. 9(9):e19808. DOI:10.1016/j.heliyon.2023.e19808

[14]Al-Ashouri, A., Köhnen, E., Li, B., et al. (2020). Monolithic perovskite/silicon tandem solar cell with >29% efficiency by enhanced hole extraction. *Science*. 370(6522):1300-1309. DOI:10.1126/science.abd4016

[15]Arbouz, H. (2024). Study of an efficient and environmentally friendly germanium-based $CsGeI_3$ perovskite structure for single and double solar cells. *International Journal of Computational and Experimental Science and Engineering*. 10(1):33-41. DOI:10.22399/ijcesen.250

[16]Lee, B., Stoumpos, C. C., Zhou, N., Hao, F., Malliakas, C., Yeh, C.-Y., Marks, T. J., Kanatzidis, M. G., & Chang, R. P. H. (2014). Air-stable molecular semiconducting iodosalts for solar cell applications: Cs_2SnI_6 as a hole conductor. *Journal of the American*

Chemical Society. 136(43):15379-15385. DOI:10.1021/ja508464w

[17]Burgelman, M., Nollet, P., & Degrave, S. (2000). Modelling polycrystalline semiconductor solar cells. *Thin Solid Films*. 361-362:527-532. DOI:10.1016/S0040-6090(99)00825-1

[18]Eperon, G. E., Leijtens, T., Bush, K. A., et al. (2016). Perovskite-perovskite tandem photovoltaics with optimized band gaps. *Science*. 354(6314):861-865. DOI:10.1126/science.aaf9717

[19]PTC Inc. (2025). *PTC Mathcad Prime 11* (Version 11) [Computer software]. https://www.mathcad.com

[20]Benmir, A., & Aida, M. S. (2013). Analytical modeling and simulation of CIGS solar cells. *Energy Procedia*. 36:618-627. DOI:10.1016/j.egypro.2013.07.073

[21]Ali, Z. M., Calasan, M., Mostafa, M. H., & Abdel Aleem, S. H. E. (2024). Analytical modeling of novel equivalent circuits of double diode solar cell circuits using a special transcendental function approach. *PLOS ONE*. 19(11):e0313713. DOI:10.1371/journal.pone.0313713

[22]Courel, M., Andrade-Arvizu, J. A., & Vigil-Galán, O. (2014). Towards a CdS/Cu_2ZnSnS_4 solar cell efficiency improvement: A theoretical approach. *Applied Physics Letters*. 105(23):233501. DOI:10.1063/1.4903826

[23]De Wolf, S., Holovsky, J., Moon, S.-J., Löper, P., Niesen, B., Ledinsky, M., Haug, F.-J., Yum, J.-H., & Ballif, C. (2014). Organometallic halide perovskites: Sharp optical absorption edge and its relation to photovoltaic performance. *The Journal of Physical Chemistry Letters*. 5(6):1035-1039. DOI:10.1021/jz500279b

[24]Lu, S., Zhou, Q., Ouyang, Y., Guo, Y., Li, Q., & Wang, J. (2018). Accelerated discovery of stable lead-free hybrid organic-inorganic perovskites via machine learning. *Nature Communications*. 9:3405. DOI:10.1038/s41467-018-05761-w

[25]Shockley, W., & Queisser, H. J. (1961). Detailed balance limit of efficiency of p-n junction solar cells. *Journal of Applied Physics*. 32(3):510-519. DOI:10.1063/1.1736034

[26]Zhang, F. (2023). The numerical simulation of CIS/CISSe graded band gap solar cell using SCAPS-1D software. *Journal of Nanoparticle Research*. 25(12):256. DOI:10.1007/s11051-023-05906-z

[27]Saif, A. A., & Alahmadi, G. (2025). Optimization of HTL and ETL materials and parameters for high-efficiency $CH_3NH_3SnI_3$ perovskite solar cells. *AIMS Materials Science*. 12(5):1004-1024. DOI:10.3934/matersci.2025046

[28]Kohnehpoushi, S., Nazari, P., Nejand, B. A., & Eskandari, M. (2018). MoS_2: A two-dimensional hole-transporting material for high-efficiency, low-cost perovskite solar cells. *Nanotechnology*. 29(20):205201. DOI:10.1088/1361-6528/aab1d4

[29]Zhang, Z., et al. (2022). Ultraviolet photocatalytic degradation of perovskite solar cells: Progress, challenges, and strategies. *Nano Energy*. 93:106812. DOI:10.1016/j.nanoen.2021.106812

[30]Zhou, Y., et al. (2021). A spiro-OMeTAD based semiconductor composite with over 100 °C glass transition temperature for durable perovskite solar cells. *Nano Energy*. 83:105655. DOI:10.1016/j.nanoen.2020.105655

[31]Gedi, S., Alhammadi, S., Noh, J., Minnam Reddy, V. R., Park, H., Rabie, A. M., Shim, J.-J., Kang, D., & Kim, W. K. (2022). SnS_2 nanoparticles and thin film for application as an adsorbent and photovoltaic buffer. *Nanomaterials*. 12(2):282. DOI:10.3390/nano12020282

[32]Wang, Q. H., Kalantar-Zadeh, K., Kis, A., Coleman, J. N., & Strano, M. S. (2012). Electronics and optoelectronics of two-dimensional transition metal dichalcogenides. *Nature Nanotechnology*. 7:699-712. DOI:10.1038/nnano.2012.193

[33]Hao, F., Stoumpos, C. C., Cao, D. H., Chang, R. P. H., & Kanatzidis, M. G. (2014). Lead-free solid-state organic–inorganic halide perovskite solar cells. *Nature Photonics*. 8:489-494. DOI:10.1038/nphoton.2014.82

[34]Yasin, S., Waar, Z. A., & Moustafa, M. (2024). Eco-friendly $KGeCl_3$ solar cells: Performance enhancement through HTL engineering. *2024 International Semiconductor Conference (CAS)*. IEEE. 91-94. DOI:10.1109/CAS62834.2024.10736857

[35]Rehman, U. U., et al. (2025). Improving efficiency of germanium-based perovskite solar cells with graphene interface layer: A strategy to minimize charge recombination. *Journal of Physics and Chemistry of Solids*. 198:112487. DOI:10.1016/j.jpcs.2024.112487

[36]Li, X., Zhao, X., Gu, Y., Yin, X., Nan, H., Tai, M., Chen, H., Shen, H., & Lin, H. (2018). Solution-processed kesterite Cu_2ZnSnS_4 as efficient hole extraction layer for inverted perovskite solar cells. *Chemistry Letters*. 47(6):817-820. DOI:10.1246/cl.180219

[37]Kumar, M. H., Dharani, S., Leong, W. L., et al. (2014). Lead-free halide perovskite solar cells with high photocurrents realized through vacancy modulation. *Advanced Materials*. 26(41):7122-7127. DOI:10.1002/adma.201401991

[38]Bush, K. A., Palmstrom, A. F., Yu, Z. J., et al. (2017). 23.6%-efficient monolithic perovskite/silicon tandem solar cells with improved stability. *Nature Energy*. 2:17009. DOI:10.1038/nenergy.2017.9

[39]Tong, J., Song, Z., Kim, D. H., et al. (2019). Carrier lifetimes of >1 μs in Sn-Pb perovskites enable efficient all-perovskite tandem solar cells. *Science*. 364(6439):475-479. DOI:10.1126/science.aav7911